Understanding the potential of a new zinc-triazolato-carbonate metal-organic framework for humid CO_2 capture processes

Ping Song,[a] Nicholas Stiles Wilkins,[a] Omid Taheri-Qazvini,[a] Adebayo A. Adeleke,[a] Alireza Lotfollahzade Moghaddam,[a] Morteza Chehel Amirani,[a] Karthik Srinivasan,[a] Nima Masoumifard,[a] and Vaidhyanathan Ramanathan*[a]

Synthesis conditions

Materials. All chemicals and reagents are commercially available and used without further purification.

Synthesis of SMOF-572 (solvothermal). 3-amino-5-methyl-triaozle (ATZM, 4mmol, 0.39g) and zinc nitrate hexahydrate (4mmol, 1.19g) were dissolved in 8ml of DMF and 32ml of water, respectively. The latter solution was poured into the former solution under stirring and kept stirring for another 20min. The solution was transferred into 100ml of Teflon reactor. The solvothermal reaction was carried out at 423K for 60 hrs. the white crystalline product were collected by filtration and thoroughly washed by methanol. After being air-dried, the product yield was 66%. Molecular formula calculated for $Zn_2(ATZM)_2(CO_3)\cdot 0.75H2O$, Calculated (%): C, 20.4; H, 3.16; N, 27.3; Found (%): C, 20.0; H, 2.67; N, 28.0.**Synthesis of SMOF-572 (water-based)**. At room temperature, 3-amino-5-methyl-1,2,4-triazole (0.5mmol, 0.050g) and pyroglutamic acid (0.5mmol, 0.065g) were added into water (10ml) and stirred for 25min (pH=3.65). Zinc carbonate basic (0.5mmol of Zn, 0.056g) were added subsequently and heated up to 65C for 1d. The white crystalline powders were collected by filtration and washed with methanol, subsequently air-dried. The product yield was 54.2%. Molecular formula calculated for $Zn_2(ATZM)_2(CO_3)\cdot 0.75H2O$, Calculated (%): C, 20.4; H, 3.16; N, 27.3; Found (%): C, 21.2; H, 2.66; N, 27.6. Note the water-based sample of SMOF-572 showed ~6cc/g lower CO2 uptake (15%CO2 323K) compared to that of solvothermal sample.

Synthesis of SMOF-537 (water-based). At room temperature, 3,5-diamino-1,2,4-triazole (DATZ, 0.5mmol, 0.050g) and pyroglutamic acid (0.25mmol, 0.032g) were added into water (10ml) and stirred for 25min (pH =4.30). Zinc carbonate basic (0.5mmol of Zn, 0.056g) were added subsequently and heated up to 65C for 1d. The white crystalline powders were collected by filtration and washed with methanol, subsequently air-dried. The product yield was 75.5%. Molecular formula calculated for $Zn_2(DATZ)_2(CO_3)\cdot 0.75H2O$, Calculated (%): C, 14.5; H, 2.66; N, 33.9; Found (%): C, 14.1; H, 2.07; N, 33.2.

Characterization methods

Single-crystal X-ray diffraction was carried out on a Bruker D8 VENTURE using Cu radiation. The data were integrated using Apex 5 software. Power X-Ray diffraction (PXRD) data was collected by Rigaku-Miniflex-600 at a scanning rate of 10°/min with Cu radiation. Thermogravimetric analysis (TGA) was conducted with a heating rate of 5°/min under nitrogen. CO_2 and N_2 isotherms were measured on Micromeritics 3Flex with evacuation at 110°C for 12hr. Water isotherms were measured on Micromeritics ASAP 2020. Fourier transform infrared spectroscopy (FTIR) was conducted with Thermo Scientific™ Nicolet™ iS50. Dynamic vapour sorption (DVS) was measured on DVS Resolution from Surface Measurement Systems Ltd.

Process Modelling Details

At Svante Technologies Inc., we use the Rapid Cycle Temperature Swing Adsorption (RCTSA) process [1] to separate CO_2 from a point-source flue gas using high-temperature, low-pressure steam. The RCTSA cycle can be simplified into three main steps and is shown in the main-body as Figs. 3A and B [1, 2]:

1. *Adsorption*: during this step, feed gas is introduced to the top of the adsorption column ($z = 0$) at the feed pressure (P_{ads}), feed temperature (T_{ads}), and feed interstitial velocity (v_{ads}), for a duration of time (t_{ads}). The aim of this step is to load the adsorbent column with CO_2, while rejecting N_2 at the bottom of the adsorption column ($z = L$). The flue gas was considered to be 15 mol% CO_2 (humid, balance N_2), at 40°C and 1.01325 bar,a.
2. *Steam Regeneration*: during this step, pure steam is introduced to the bottom of the adsorption column ($z = L$) at the steam pressure (P_{stm}), temperature (T_{stm}), and interstitial velocity (v_{stm}), for a duration of time (t_{stm}). The aim of this step is to remove the CO_2 loaded during the adsorption step and concurrently rejecting N_2 at the top of the adsorption column ($z = 0$). This step was operated at a temperature greater than 100°C and a pressure of 1.01325 bar,a.
3. *Air Conditioning*: during this step, conditioned air is introduced to the top of the adsorption column ($z = 0$) at the conditioning pressure (P_{cond}), temperature (T_{cond}), and interstitial velocity (v_{cond}), for a duration of time (t_{cond}). The aim of this step is to remove the steam loaded during the steam regeneration step and concurrently cooling the adsorbent column. This step was considered to contain humid N_2 at a temperature less than 100°C and a pressure of 1.01325 bar,a.

The RCTSA process was simulated in a built in-house adsorption process simulator first described by Haghpanah et al. for pressure-vacuum swing adsorption systems [3]. This simulator solves the coupled partial-differential equations that describe the mass and energy balances across the adsorption column [3]. The process simulator has since been extended to model pressure, vacuum, and temperature swing steps [2]. This simulator approximates the adsorption column in one spatial (axial) dimension using finite volume techniques. In particular, 40 volumes were used with the van Leer flux limiter. The model equations are given in Table 1. The simulator assumes the following:

1. The gas phase is ideal. This assumption is justified since the associated gas compressibility factors are all close to 1.000. Specifically, the compressibility of low-pressure steam is within 1.3% of ideality ($z = 1.000 \pm 0.013$) using predictions from the IAPWS 1995 equation of state [4].
2. The column is one-dimensional with no radial gradients in temperature or concentration.
3. Axially dispersed plug flow describes the flow in the column.
4. Darcy's law adequately describes the pressure drop in the column.
5. The solid and gas phases achieve thermal equilibrium instantaneously.
6. The column properties are isotropic.
7. The linear driving force (LDF) model describes mass transfer in the column. This assumption is justified since the effective pore size of CALF-20 (≈ 4.0 Å along the square channel diagonal) and SMOF-572 (≈ 3.9 Å) are larger than the kinetic diameters of CO_2 (3.30 Å), N_2 (3.64 Å), and H_2O (2.65 Å).

Table S1: Equations to model adsorption dynamics. Nomenclature for these equations: t is the time, z is axial distance, P is the total pressure, T is the temperature, v is the interstitial velocity, R is the universal gas constant, y_i is the mole fraction, q_i is the solid-phase loading, q_i^* is the equilibrium solid-phase loading, ρ is the density, ϵ is the bed void fraction, D_L is the effective axial dispersion, k_i is the mass transfer coefficient, c_f is a proportionality constant, μ is the fluid visocity, $t_{h,L}$ is the half laminate thickness, C_p is the specific heat capacity, K is the effective conductivity, $\bar{r}_{in}$ and $\bar{r}_{out}$ are the effective inner and outer contactor wall radiuses, h_{in} and h_{out} are the inner and outer heat transfer coefficients, and $\Delta H_{iso,i}$ is the isosteric heat of adsorption. The subscript a denotes the adsorbed-phase, amb denotes ambient, g denotes the gas-phase, i denotes component i, s denotes the solid, w denotes the contactor wall.

Overall Mass Balance	$\frac{1}{P}\frac{\partial P}{\partial t} - \frac{1}{T}\frac{\partial T}{\partial t} = -\frac{T}{P}\frac{\partial}{\partial z}\left(\frac{P}{T}v\right) - \frac{RT}{P}\frac{1-\epsilon}{\epsilon}\sum_{i=1}^{n_{\text{comp}}}\frac{\partial q_i}{\partial t}$
Component Mass Balance	$\frac{\partial y_i}{\partial t} + \frac{y_i}{P}\frac{\partial P}{\partial t} - \frac{y_i}{T}\frac{\partial T}{\partial t} = D_{\text{L}}\frac{T}{P}\frac{\partial}{\partial z}\left(\frac{P}{T}\frac{\partial y_i}{\partial z}\right) - \frac{T}{P}\frac{\partial}{\partial z}\left(\frac{y_i P}{T}v\right) - \frac{RT}{P}\frac{1-\epsilon}{\epsilon}\frac{\partial q_i}{\partial t}$
Solid Phase Mass Balance	$\frac{\partial q_i}{\partial t} = k_i(q_i^* - q_i)$
Pressure Drop	$-\frac{\partial P}{\partial z} = c_f\frac{\mu v}{t_{h,L}^2}\left(\frac{1-\epsilon}{\epsilon}\right)^2$
Wall Energy Balance	$\rho_{\text{w}}C_{p,\text{w}}\frac{\partial T_{\text{w}}}{\partial t} = K_{\text{w}}\frac{\partial^2 T_{\text{w}}}{\partial z^2} + \frac{2\bar{r}_{\text{in}}\text{h}_{\text{in}}}{\bar{r}_{\text{out}}^2 - \bar{r}_{\text{in}}^2}(T - T_{\text{w}}) - \frac{2\bar{r}_{\text{out}}\text{h}_{\text{out}}}{\bar{r}_{\text{out}}^2 - \bar{r}_{\text{in}}^2}(T_{\text{w}} - T_{\text{amb}})$
Column Energy Balance	$\left[\frac{1-\epsilon}{\epsilon}\left(\rho_{\text{s}}C_{p,\text{s}} + C_{p,\text{a}}\sum_{i=1}^{n_{\text{comp}}}q_i\right)\right]\frac{\partial T}{\partial t} =$ $\frac{K_{\text{w}}}{\epsilon}\frac{\partial^2 T}{\partial z^2} - \frac{C_{p,\text{g}}}{R}\frac{\partial}{\partial z}(vP) - \frac{C_{p,\text{g}}}{R}\frac{\partial P}{\partial t} - \frac{1-\epsilon}{\epsilon}C_{p,\text{a}}T\sum_{i=1}^{n_{\text{comp}}}\frac{\partial q_i}{\partial t} + \frac{1-\epsilon}{\epsilon}\sum_{i=1}^{n_{\text{comp}}}\left[\left(-\Delta H_{\text{iso},i}\right)\frac{\partial q_i}{\partial t}\right] - \frac{2\text{h}_{\text{in}}}{\epsilon\bar{r}_{\text{in}}}(T - T_{\text{w}})$
Dual-Site Langmuir Isotherm	$q_i^* = \frac{q_{b,i}^{\text{sat}}b_i C_i}{1 + b_i C_i} + \frac{q_{d,i}^{\text{sat}}d_i C_i}{1 + d_i C_i}$
Van't Hoff Relationship	$b_i = b_{0,i}\exp\left(\frac{-\Delta U_{b,i}}{RT}\right)\ \&\ d_i = d_{0,i}\exp\left(\frac{-\Delta U_{d,i}}{RT}\right)$

RCTSA process performance is evaluated through many adsorption process metrics, including the process purity (Pu), recovery (Rec), and productivity (Pr). The (dry) CO_2 purity can is defined below:

$$\text{Pu} = \frac{n_{\text{CO}_2}^{\text{steam,out}}}{n_{\text{CO}_2}^{\text{steam,out}} + n_{\text{N}_2}^{\text{steam,out}}} \quad (1)$$

CO_2 is only captured during the steam regeneration step. Therefore, the (dry) CO_2 purity contains only the effluent CO_2 ($n_{\text{CO}_2}^{\text{steam,out}}$) and N_2 ($n_{\text{N}_2}^{\text{steam,out}}$) molar quantities in its calculation.

The CO_2 recovery is defined as:

$$\text{Rec} = \frac{n_{\text{CO}_2}^{\text{steam,out}}}{n_{\text{CO}_2}^{\text{ads,in}}} \quad (2)$$

CO_2 only enters the process in the flue gas during the adsorption step and is only collected as a product in the steam regeneration step. Therefore, we only require the inlet CO_2 from the adsorption step ($n_{\text{CO}_2}^{\text{ads,in}}$) and the effluent CO_2 from the steam regeneration step ($n_{\text{CO}_2}^{\text{steam,out}}$).

The productivity (in tonnes CO_2 day^{-1} m^{-3}) is defined as:

$$\text{Pr} = \frac{m_{\text{CO}_2}^{\text{steam,out}}}{V_{\text{adsorbent}}t_{\text{cycle}}} \quad (3)$$

Where $m_{CO_2}^{steam,out}$ is the mass of CO_2 captured in the steam regeneration step, $V_{adsorbent}$ is the volume of the adsorbent, and t_{cycle} is the duration of the adsorption process cycle. t_{cycle} is the sum of all constituent step times: $t_{cycle} = t_{ads} + t_{steam} + t_{cond}$. While the volume of adsorbent was fixed (per considered adsorbent), the cycle time and quantity of captured CO_2 was variable across different simulations and materials.

All process performance metrics are reported at cyclic-steady state. In this study, cyclic steady state was defined as any cycle that achieved at least 60 process cycles with a CO_2 mass balance error $\leq 1.5\%$. The second inequality is given in the following equation:

$$\frac{n_{CO_2,in} - n_{CO_2,out}}{n_{CO_2,in}} \cdot 100\% \leq 1.5\% \quad (4)$$

The dual-site Langmuir isotherm was sufficient to approximate the CO_2 and H_2O adsorption equilibrium data (all display type-1 isotherm trends). The N_2 data was fitted to a single-site Langmuir isotherm. These were extended into a multitemperature isotherm fit via the Van't Hoff relationship. All isotherm fits were made in terms of concentration [mol/m^3] ($C_i = P_i/RT$) to the powder/crystalline MOF adsorbent. However, process simulations considered a dereated (or weakened) isotherm to reflect the adsorbent-lamination process (the adsorbent contactor is a structured laminate-bed). Similar to a pelletization process with binder, the expected laminate-based loading will be less than the as-synthesized loadings. The isotherms utilized in the process were reduced by a constant factor. Competitive adsorption data was measured with a gravimeter and fitted as a function of relative humidity. This function takes the form:

$$\frac{q^*_{CO_2,wet}}{q^*_{CO_2,dry}} = \exp(-c_1 x^{c_2}) \quad (5)$$

where c_1 and c_2 are constants fitted to the experimental data, x is the fractional relative humidity (unitless), $q^*_{CO_2,wet}$ is the 'humid' CO_2 loading, and $q^*_{CO_2,dry}$ is the unary, or 'non-humid', loading. This function can then be multiplied to the CO_2 isotherm to approximate humid CO_2 uptake. The approach has been utilized in other adsorptive process studies to simplify the estimation of CO_2 and H_2O multicomponent equilibrium.

Selectivity Calculation Details

The ideal adsorbed solution theory selectivity for CO_2 to N_2 (α_{CO_2/N_2}) was calculated using the following equations:

$$\alpha_{CO_2/N_2} = \frac{q^*_{CO_2}/q^*_{N_2}}{y_{CO_2}/y_{N_2}} \quad (6)$$

If the single-site Langmuir isotherm is assumed for both components:

$$q_i^* = \frac{q_b^{sat} b_i C_i}{1 + b_i C_i} \quad (7)$$

Where: q_i^* is the equilibrium loading of component i, C_i is the concentration of i, q_b^{sat} is the saturation capacity of the adsorbent, and b_i is the component nonlinearity parameter (a function of temperature). Equation 6 reduces to:

$$\alpha_{CO_2/N_2} = \frac{b_{CO_2}}{b_{N_2}} \quad (8)$$

The nonlinearity parameter can be fitted to a Van't Hoff type expression:

$$b_i = b_{0,i} \exp\left(\frac{-\Delta U_{b,i}}{RT}\right) \quad (9)$$

Where $b_{0,i}$ is the exponential prefactor, $\Delta U_{b,i}$ is the internal energy of adsorption, T is the temperature, and R is the universal gas constant. Applying these equations, the following IAST selectivities can be found. These values were calculated for a 15/85 mol% mixture of CO_2 and N_2 at temperatures between 0 and 100°C for both CALF-20 and SMOF-572.

Characterizations

Single crystal structural data

Table S2. Crystallographic Information for SMOF-537 and SMOF-572

	SMOF-537	SMOF-572
a/Å	17.5131(16)	17.5097(3)
b/Å	8.7986(7)	8.9985(2)
c/Å	9.6977(7)	9.9050(2)
α/°	90	90
β/°	105.755(6)	108.7290(10)
γ/°	90	90
V/Å3	1438	1478
Crystal System	monoclinic	monoclinic
Space Group	C 2/c	C 2/c
Color	Colourless	Colourless
Z	4	4
T/ K	100	273
Diffraction Source	Cu	Cu
Diffraction radiation wavelength/ Å	1.54	1.54
R1, wR2 (all data)	0.0665, 0.1477	0.0393, 0.1468
R-Factor %	6.65	3.85

Computational details and structure modelling

Grand canonical Monte Carlo (GCMC): Gas adsorption simulations were carried out via the grand canonical Monte Carlo (GCMC) calculations performed in RASPA-2.0 code [6]. In the GCMC simulations, insertion, deletion, and translation and rotation moves were attempted with equal probability. The interactions between the gas species and the framework were modeled using Lennard–Jones (LJ) plus Coulomb potentials. LJ parameters for all atoms in MOFs were taken from Dreiding force field (DFF) [7] and were truncated at a cutoff radius of 12.8 Å. The Lorentz-Berthelot mixing rules were used to calculate cross interactions. Partial atomic charges for SMOF-572 were calculated using the REPEAT (Repeating Electrostatic Potential Extracted Atomic) method [8] and the Ewald summation technique was used to calculate electrostatic interactions. GCMC simulations for CO_2 adsorption were run for 20,000 cycles for equilibration and a further 20,000 cycles to average properties. CO_2 was modeled using the TraPPE model [9].

Density Functional Theory (DFT): To investigate how CO_2 interacts with the SMOF-572 framework during adsorption, we adopted a combined quantum-classical strategy integrating density functional theory (DFT) and molecular dynamics (MD) simulations. All electronic-structure calculations were carried out with the FHI-aims package [10], employing the Perdew–Burke–Ernzerhof (PBE) functional within the generalized gradient approximation (GGA) for exchange-correlation effects [11]. Both Framework atoms and the CO_2 adsorbate were described with a numerically tabulated atom-centered basis of tier-2 quality, which introduces diffuse function to achieve high fidelity in energy evaluation. Long-range dispersion was explicitly incorporated via the exchange-dipole moment (XDM) correction scheme applied post self-consistency [12-13]. Reciprocal space integration was performed with a Monkhorst-Pack mesh of 3x5x5, and the forces were optimized until they were below 0.1 meV/Å. For stringent electronics accuracy, the charge density integration parameter was fixed at sc_accuracy_rho = 1x10-7. The binding energy was obtained from the total energies of three states: the isolated CO_2 molecule (the guest), the relaxed SMOF-572 framework (the host), and the fully equilibrated host-guest complex.

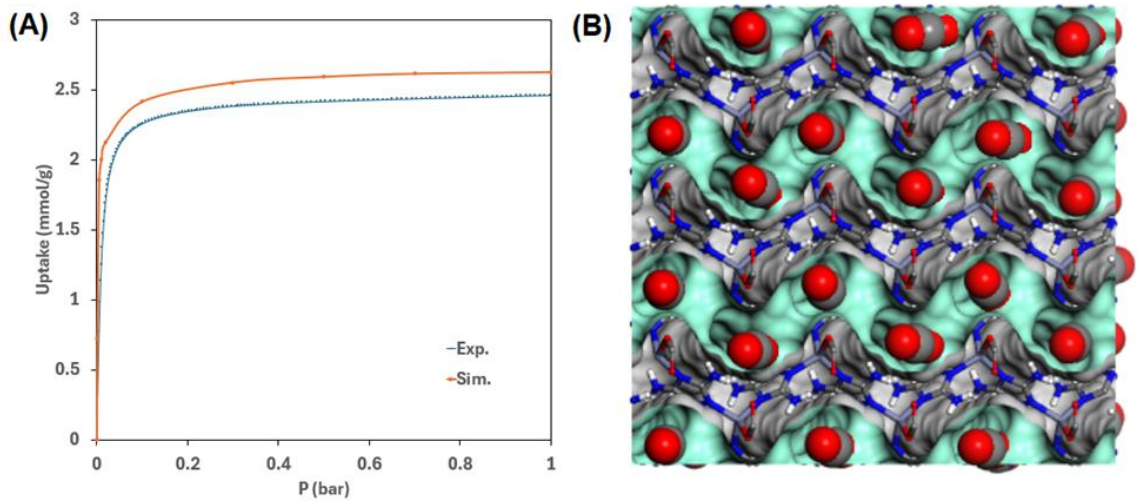

Figure S1. (a) CO_2 simulated isotherms using GCMC compared to experimental isotherm at 273 K showing good match. (b) Location of CO_2 guest molecules inside the pores at 1 bar and 273 K derived from GCMC simulation.

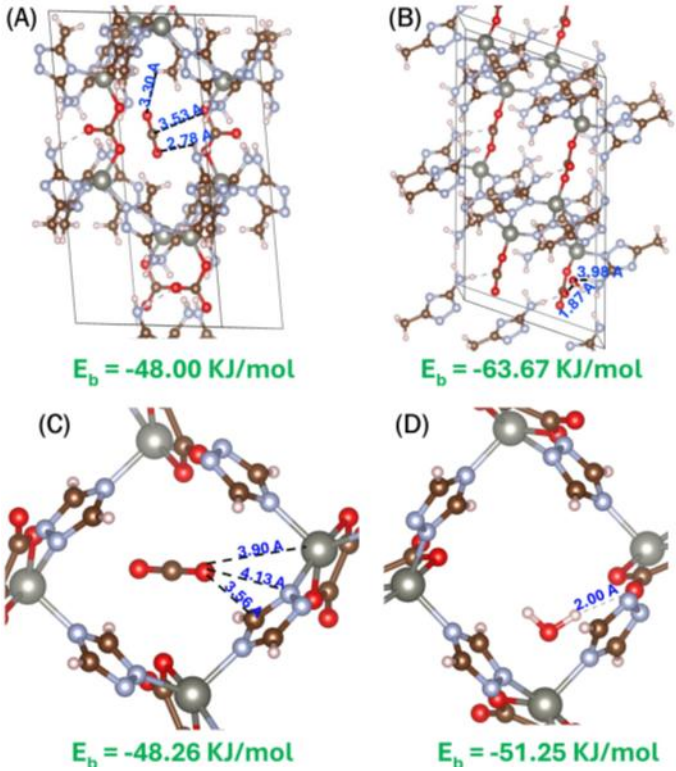

Figure S2. DFT-assisted identification of the location of (A) CO_2 (B) water in SMOF572, and DFT-assisted identification of the location of (C) CO_2 (D) water in CALF-20 at an identical level of theory.

Bulk characterizations:

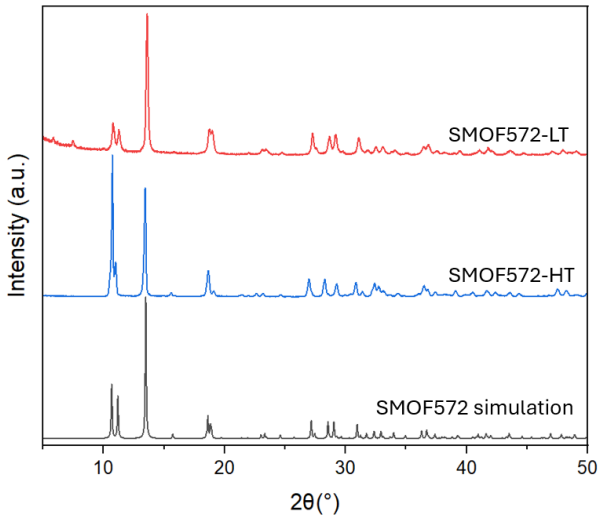

Figure S3. PXRD of SMOF-572 samples: simulation, solvothermal synthesis with DMF, and water-based synthesis.

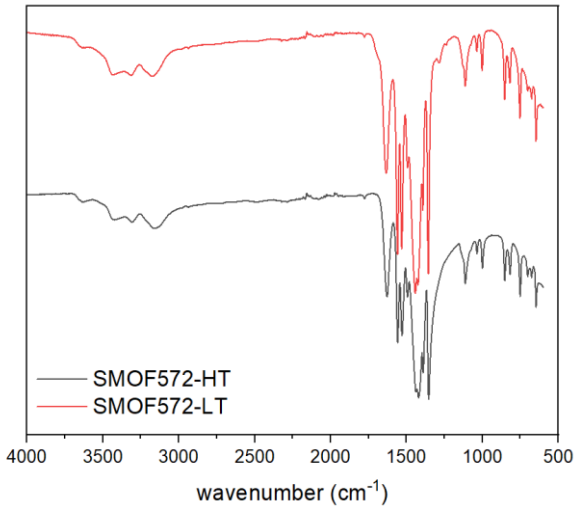

Figure S4. FTIR of SMOF-572 samples synthesized from water-based (SMOF572-LT) and solvothermal method (SMOF572-HT)

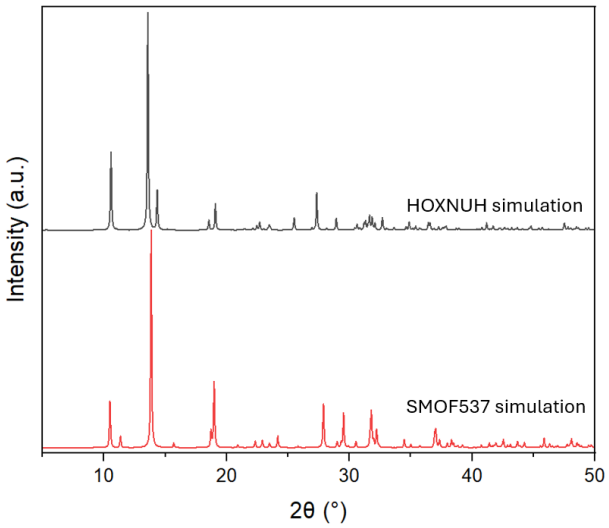

Figure S5. Simulated PXRD of SMOF537 and HOXNUH.

Note: Another Zn-CO_3-DATZ phase was recently reported with Zn-3,5-diamino-triazolate layers and carbonate as a pillar for ethylene separation [5] (CCDC code HOXNUH), which is compared with the SMOF-537 structure in this work. The angles between carbonate pillars are more open for SMOF-537 in this work, which led to its bigger pores and higher CO_2 uptake.

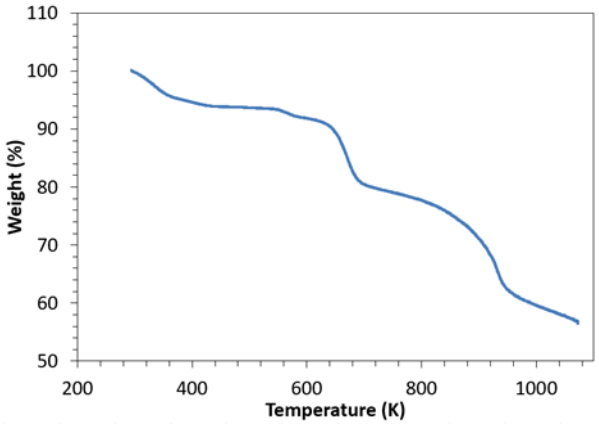

Figure S6. TGA curve of SMOF-572 under N_2.

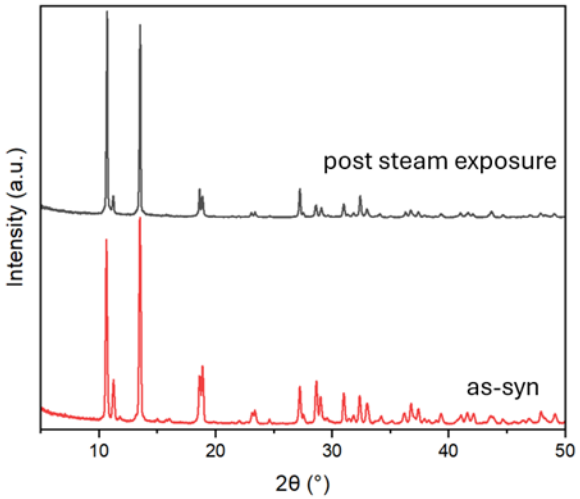

Figure S7. PXRD of SMOF-572 as-synthesized and after 3 days of steam exposure.

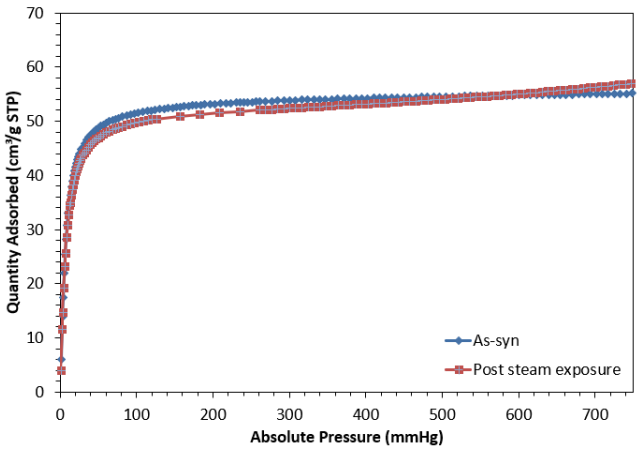

Figure S8. CO2 isotherms of SMOF-572 as synthesized and post steam exposure at 273K.

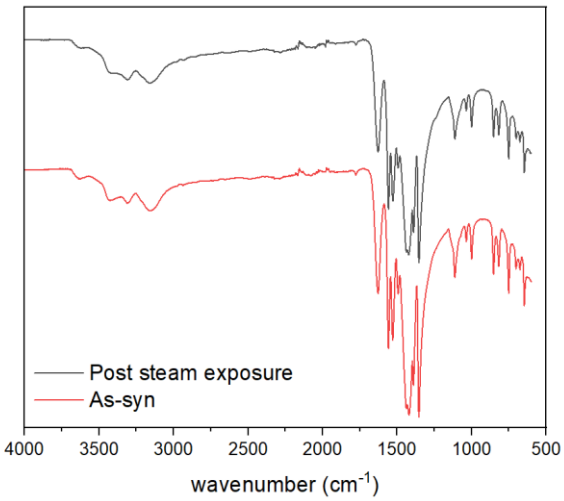

Figure S9. FTIR spectra of SMOF-572 as-synthesized and after 3 days of steam exposure.

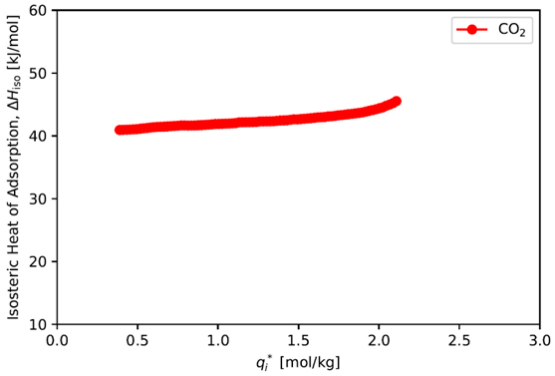

Figure S10. CO_2 heat of adsorption for SMOF-572.

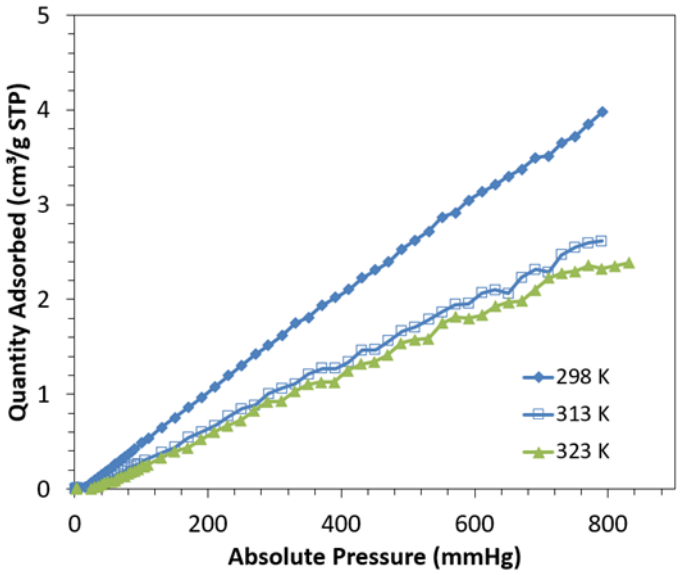

Figure S11. N2 isotherms of SMOF-572 at 293, 313, and 323K.

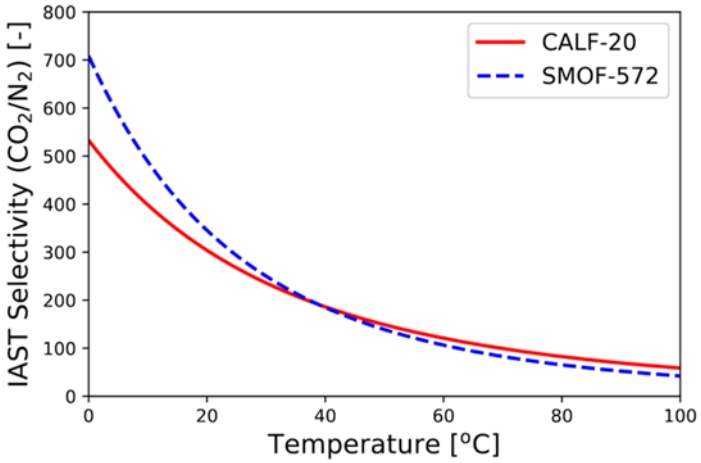

Figure S12. IAST selectivities calculated for a 15/85 mol% mixture of CO_2 and N_2 at temperatures between 273 and 373K.

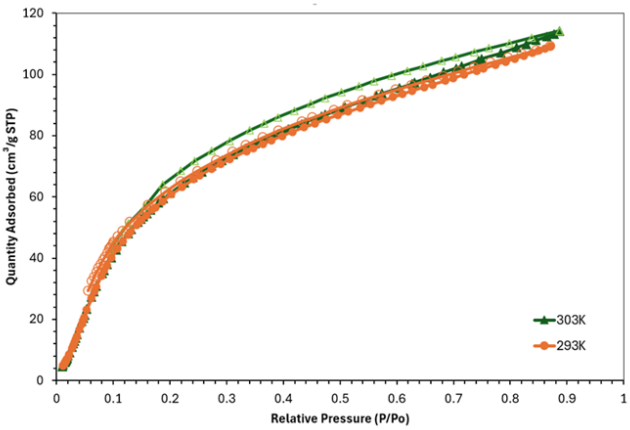

Figure S13. Water isotherms of SMOF-572 at 293 and 303K.

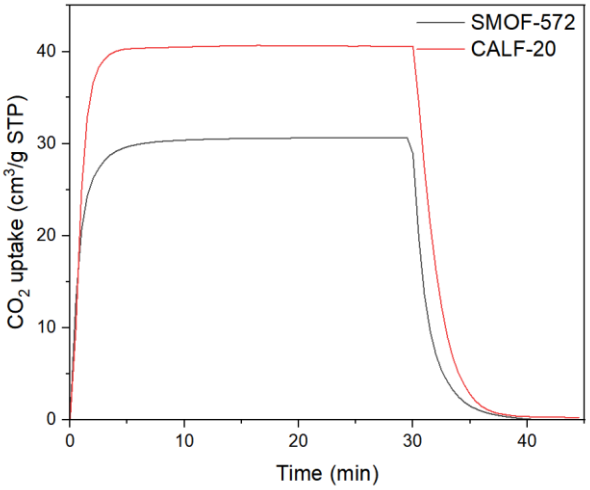

Figure S14. TGA of CO2 adsorption (15%CO2, 85%He) and desorption curves (100%He) with time at 323K: SMOF-572 and CALF-20.

References

1. S. Rezaei, A. Liu and P. Hovington, Catalysis Today, 2023, 423, 114286.
2. N. S. Wilkins, M. Hashem, K. N. Pai, S. Rezaei, M. Neisiani and P. Hovington, Proceedings of the 17th International Conference on Greenhouse Gas Control Technologies, 2024.
3. R. Haghpanah, A. Majumder, R. Nilam, A. Rajendran, S. Farooq, I.A. Karimi and M. Amanullah, Industrial & Engineering Chemistry Research, 2013, 52(11), 4249.
4. W. Wagner and A. Pruss Journal of Physical and Chemical Reference Data, 2002, 31(2), 387-535
5. Jin-Bo Wang, Tao Zhang, Jian-Wei Cao, Rong Yang, Su-hang Wang, Xue Zhang, and Kai-Jie Chen. Inorganic Chemistry 2024 63 (37), 17298-17304

6. D. Dubbeldam, S. Calero, D. E. Ellis and R. Q. Snurr, Molecular Simulation, 2016, 42.2, 81-101

7. S. L. Mayo, B. D. Olafson, and W. A. Goddard, Journal of Physical Chemistry, 1990, 94(26), 8897-8909

8. M. Krykunov, C. Demone, J. W. H. Lo and T. K. Woo, Journal of Chemical Theory and Computation, 2017, 13(6), 2858-2869

9. P. Bai, M. Tsapatsis and J. I. Siepmann, Journal of Physical Chemistry C, 2013, 117(46) 24375-24387

10. V. Blum, R. Gehrke, F. Hanke, P. Havu, V. Havu, X. Ren, K. Reuter and M. Scheffler, Computer Physics Communications, 2009, 180(11), 2175-2196

11. J. P. Perdew, K. Burke and M. Ernzerhof, Physical Review Letters, 1996, 77, 3865

12. A. D. Becke and E. R. Johnson, Journal of Chemical Physics, 2005, 122, 154104

13. E. R. Johnson and A. D. Becke, Journal of Chemical Physics, 2005, 123, 024101